nature communications

Article

https://doi.org/10.1038/s41467-026-70336-z

Single-cell thiol profiling enabled by live-cell labeling reveals metabolic heterogeneity in ferroptosis

Received: 31 July 2025

Accepted: 25 February 2026

Published online: 03 March 2026

Check for updates

Daiyu Miao[1], Qiuning Li[1], Yi Zhang[1], Shaojie Qin[1], Ying Wang[2], Xiaoyun Liu[2] & Yu Bai[1]

Thiols serve indispensable biochemical functions across catalysis, redox homeostasis and energy metabolism. However, profiling multiple thiols at the single-cell level remains challenging due to their trace amount and susceptibility to oxidation. Herein, we report an integrated strategy for thiol profiling at the single-cell level which combines live-cell labeling with organic mass cytometry. The live-cell labeling strategy facilitates the comprehensive measurement of intrinsic thiols with expanded coverage and improved sensitivity, while organic mass cytometry enables simultaneous quantification of 27 labeled thiols and 355 other metabolites from single cells. Assessment of metabolic fluctuation upon stimulation demonstrates practicability and accuracy of this integrated methodology which is capable of pathway activity monitoring, metabolic network mapping and untargeted metabolome profiling. Further application of this method in investigating RSL3-triggered ferroptosis reveals that RSL3 inhibits glutathione synthesis via nuclear factor E2-related factor 2- glutathione axis and results in heterogenous glutathione metabolism between subtypes.

Single-cell metabolomics reveals the phenotypic differences of heterogeneity under physiological conditions by analyzing endogenous metabolite molecules. Compared with other metabolites, endogenous reactive species facilitate the efficient functioning of biochemical processes, and their specialization ensures the coordinated and orderly integration of distinct pathways. Sulfhydryl-containing metabolites, namely thiols, play unique and pivotal roles in biological systems in virtue of their intrinsically high reducibility and nucleophilicity. For example, glutathione (GSH) maintains redox homeostasis within cells; coenzyme A (CoA) is universally involved in metabolism of lipids, amino acids, and carbohydrates; cysteine (Cys) and hydrogen sulfide function at the key node of synthesis and conversion between a diverse array of sulfur-containing species, proteins included. Dysregulation of thiol metabolism leads to oxidative stress and other metabolic dysfunctions, which are directly implicated in neurodegeneration[1], cardiovascular diseases[2], and cancer[3]. Especially, GSH depletion triggers ferroptosis, a form of regulated cell death driven by iron-dependent lipid peroxidation[4], which has drawn mounting attention since its coinage in 2012. Modulating thiol metabolism to trigger or restrain ferroptosis provides a promising strategy for cancer therapy and prevention of ischemia-reperfusion injury[5,6].

Assessment of endogenous thiols levels aids in mapping broad yet exquisite pathways in energy metabolism, homeostasis, and signaling, considering the ubiquity of sulfhydryl-containing metabolites. However, thiols are prone to oxidation when biological samples are exposed to air during preparation and detection[7,8], compromising measurement accuracy. Although reductants like tris(2-carboxyethyl)phosphine (TCEP) can regenerate thiols from disulfides[9], the formation of higher oxidation states, sulfonate, is irreversible through most moderate reactions[10]. To address this dilemma,

[1]Beijing National Laboratory for Molecular Sciences, Key Laboratory of Bioorganic Chemistry and Molecular Engineering of Ministry of Education, College of Chemistry and Molecular Engineering, Peking University, Beijing, China. [2]Department of Microbiology and Infectious Disease Center, NHC Key Laboratory of Medical Immunology, School of Basic Medical Sciences, Peking University Health Science Center, Beijing, China. e-mail: yu.bai@pku.edu.cn

https://doi.org/10.1038/s41467-026-70336-z

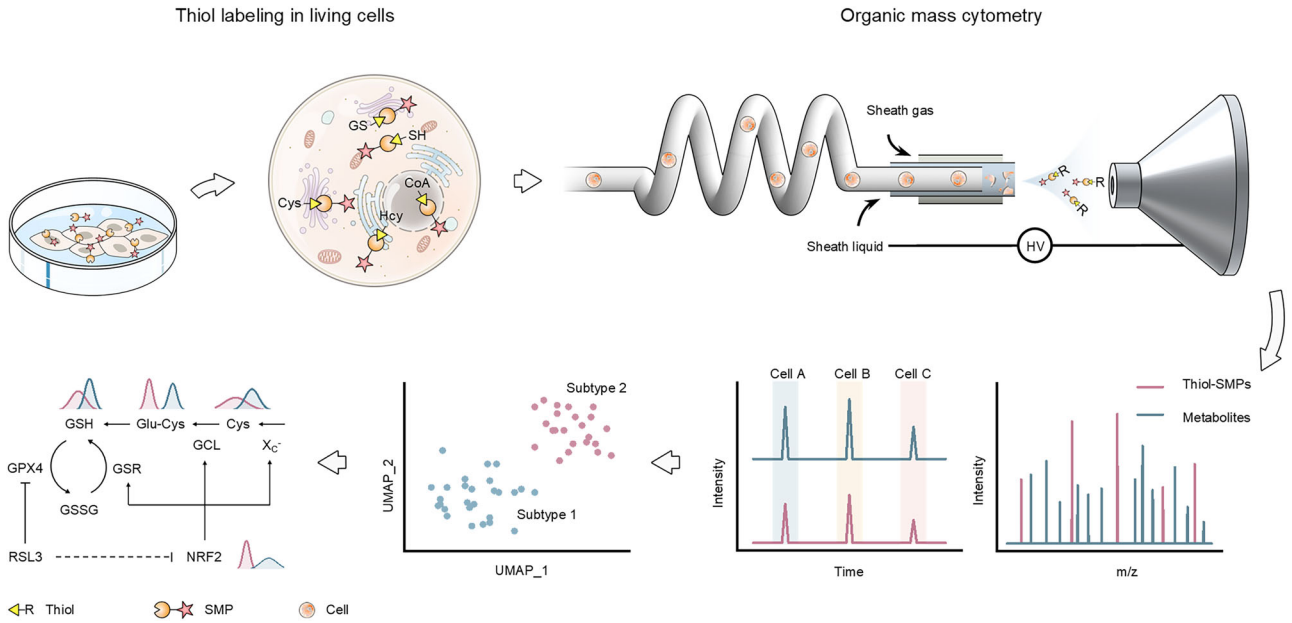

Fig. 1 | Schematic workflow of thiol profiling. Endogenous thiols are labeled by SMPs within living cells, and the cells are mono-dispersed and injected into the organic mass cytometry. Labeled thiols and other metabolites are simultaneously detected from individual living cells for shedding light on cellular heterogeneity in thiol and global metabolism.

enormous derivatization strategies that sulfhydryl-reactive probes sheltered thiols from oxidation were developed and coupled with fluorescence or mass spectrometry (MS) for thiol profiling. Though there are considerable merits of fluorescence-based approaches in convenience, sensitivity and imaging capability[11], their utility in the thiol metabolism pathway is limited by spectral overlap, which restricts metabolite coverage. MS excels at detecting multiple molecules simultaneously as well as structure identification and hence meets the requirements of pathway analysis. Nevertheless, oxidation was not completely averted in conventional MS-based approaches, which in most cases labeled thiols in cell lysates[12]. During lysis, uncaged thiols reacted with oxidizing species stemming from atmosphere, pulsed sonication and disordered biochemical reactions. These side-reactions posed severe challenges to data reliability and further impeded the in-depth investigation of thiol metabolism. On the contrary, the live-cell labeling strategy cages target molecules in the native cellular context, offering a promising avenue for the accurate interpretation of intrinsic thiol levels.

Population-averaged measurements generally mask cellular heterogeneity, whereas single-cell analysis is capable of distinguishing cell subtypes and functional variations[13,14]. Tremendous efforts have been devoted to the exploitation of metabolomics profiling at the single-cell level, which could be categorized into microsampling-mass spectrometry[15–17], mass spectrometry imaging[18–20], organic mass cytometry[21,22], etc. Among them, organic mass cytometry shows dominant advantages in operational convenience, metabolite coverage and analysis speed. It arose from conventional mass cytometry (CyTOF) which profiles proteins in the form of metal tags[23]. In organic mass cytometry, the ionization source was altered from inductively coupled plasma (ICP) to electrospray ionization (ESI) for direct detection of metabolites[24]. Recently, diverse methodologies based on organic mass cytometry for multimodal[25], in-depth[26], and dynamic[27] single-cell analysis have been developed. Considering its splendid performance, the involvement of organic mass cytometry into thiol detection is promising to shed light on heterogeneity underlying thiol metabolism.

Herein, we present a method for single-cell thiol profiling, which integrated live-cell labeling with organic mass cytometry (Fig. 1). Sulfhydryl-reactive mass spectrometry probes (SMPs) are designed and introduced into living cells to block thiols in situ as a precaution against oxidation. After labeling, cells are mono-dispersed and orderly injected into ESI-mass spectrometer. Thiol-chromene click chemistry[28] and charged labels empower SMPs to label endogenous thiols within 10 min and increase the sensitivity and coverage by magnitudes. Using the organic mass cytometry platform, we simultaneously detect multiple thiol species and other metabolites in each single cell, enabling integrated analysis of thiol metabolism and global metabolic activity at the single-cell level. The fluctuation at each node of GSH synthesis is successfully monitored, which proves the practicability and accuracy of this method. Application of this method in RSL3-triggered ferroptosis reveals that RSL3 inhibits GSH synthesis by downregulating nuclear factor E2-related factor 2 (NRF2). Meanwhile, two subtypes of RSL3-treated cells are discriminated and characterized with heterogenous GSH metabolism and lipid metabolism resulting from bimodal distribution of NRF2.

Results

Thiol labeling in living cells

We reasoned that the eligible SMP possessed conspicuous reactivity towards free sulfhydryl groups as well as sufficient biocompatibility and high MS sensitivity. The Chromene derivative, 3,3a-dihydrocyclopenta[*b*]chromen-1(2*H*)-one, was reported to cage sulfhydryl within 3 min[29] by ring-opening accelerated Michael addition (Fig. 2a) and has been utilized to visualize total thiols in living organism[30]. The efficient reactivity towards thiols and good biocompatibility rendered it a potential reactive group of SMP for single-cell thiol profiling. To enhance MS signals, the commonly used sensibilizing groups—tertiary and quaternary ammoniums—were selected as candidates of the charged labels. Accordingly, two SMPs consisting of chromene derivative and organic ammonium were designed and synthesized through a two-step or three-step route (Supplementary Fig. 1). Their efficiency was subsequently assessed at the population level (Fig. 2b) using ultra-performance liquid chromatography-mass spectrometry (UPLC-MS) with **SMP2**-labeled *N*-acetylcysteine amide (NACA) as the internal standard (IS). The same concentration of SMPs presented comparable ratio of chromatographic peak area in vitro, suggesting their similar

https://doi.org/10.1038/s41467-026-70336-z

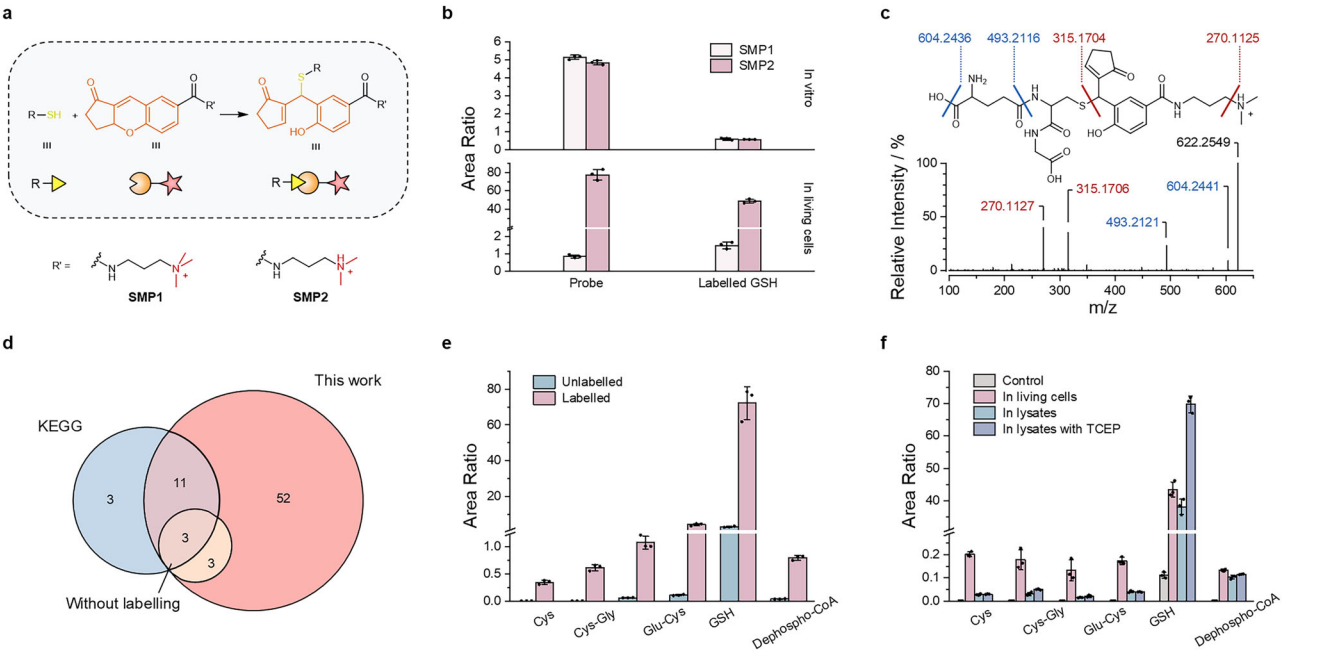

Fig. 2 | Development and evaluation of the live-cell thiol labeling strategy. **a** Thiol-chromene click chemistry and structures of SMPs. **b** Labeling efficiency of two SMPs in vitro and in living cells. Data represents mean ± s.d. (n = 3 independent experimental replicates for labeling in vitro and n = 3 biological replicates for labeling in living cells). **c** MS/MS spectrum annotation of **SMP2** labeled GSH. Pink and blue annotations represent ions originated from fragmentations of the **SMP2** residue and the GSH residue, respectively. **d** Comparison of thiol coverage among this work (pink), approaches without labeling (blue) and the KEGG pathways database (yellow): sulfur metabolism, cysteine and methionine metabolism, pantothenate and CoA metabolism, taurine and hypotaurine metabolism, and glutathione metabolism. **e** Comparison of UPLC-MS responses of **SMP2**-labeled and -unlabeled thiols from bulk cells. Data represents mean ± s.d. (n = 3 biological replicates). Gly-Cys Cysteinylglycine, Glu-Cys γ-glutamylcysteine. **f** Effect of labeling condition: in living cells and in lysates with or without TCEP. Data represents mean ± s.d. (n = 3 biological replicates). In (**b**, **e**, **f**), area ratio is calculated as the ratio of chromatographic peak area of the analyte to that of IS (SMP2-labeled NACA). Source data are provided as a Source data file.

sensitivities; this was also true of their GSH derivatives. However, SMP2 and its derivative presented substantially higher levels than those of SMP1 in living cells. This discrepancy might be attributed to their difference in membrane permeability, considering that **SMP2** (calculated octanol-water partition coefficient (cLog$P$) = 1.50) diffused across the plasma membrane more easily than excessively hydrophilic **SMP1** (cLog$P$ = −2.78). Thus, **SMP2** was selected as the optimal probe for following thiol labeling.

We subsequently optimized the treatment conditions to equilibrate labeling efficiency and biocompatibility. Given that GSH was the most abundant intracellular thiol[31], labeled GSH was chosen as the evaluation indicator for labeling efficiency. Cells were treated with varying concentration of **SMP2** for 1 h, and labeled GSH were quantified with the approach described above. In this manner, 80 μM was found to be the extreme point of treatment concentration, whereas higher concentration of **SMP2** resulted in a slight decrease (Supplementary Fig. 2a). Time-wise, labeling efficiency at 80 μM elevated with the increasing treatment time and reached a plateau at 10 min (Supplementary Fig. 2b). Cytotoxicity was evaluated synchronously with the above optimization. Cell viability maintained higher than 90.9% when the treatment concentration was ≤80 μM, whereas it dropped to 74.2% at the concentration of 100 μM (Supplementary Fig. 3a), which was responsible for the corresponding decrease of labeling efficiency. As treatment time were further shortened to 10 min, a higher cell viability of 98.3% was realized (Supplementary Fig. 3b), indicating no notable cytotoxicity induced by **SMP2**. Altogether, treating living cells with 80 μM **SMP2** for 10 min was confirmed as the optimal condition with the highest labeling efficiency and proven biocompatibility.

To identify labeled thiols, we established a thiol library initially from bulk cells. Both cancer (HeLa) and normal (NE-4C) cells were treated with **SMP2**, and polar extracts from their lysates were separately analyzed with ultra performance liquid chromatography-tandem mass spectrometry (UPLC-MS/MS). MS/MS fragmentation patterns were studied to distinguish labeled thiols from other metabolites and pinpoint their refined structures. Taking GSH as an example (Fig. 2c), characteristic ions at m/z 315.1705 and m/z 270.1127 which originated from **SMP2** indicated the corresponding molecule as a labeled thiol, while rest fragment ions at m/z 493.2121 and 604.2441 assigned it exactly to GSH. This approach was then verified by checking MS behaviors of 12 thiol standards (Supplementary Fig. 4). In this manner, 265 ions carrying **SMP2**-characteristic signatures were detected in diverse adduct forms, and ultimately 69 thiol species were identified (Supplementary Data 1). This represented a 5- to 69-fold increase in coverage as compared with fluorescent or traditional MS-based methods[11,32]. To the best of our knowledge, this is the first time that all the thiols involved in synthesis of GSH and CoA were simultaneously detected. This library shares 14 thiols with Kyoto Encyclopedia of Genes and Genomes (KEGG) database, while 55 thiols are absent in KEGG (Fig. 2d), due to being unreported or functionally uncharacterized. We surprisingly found that there were multifarious modifications of GSH and Cys, including glycosylation, lactylation and phoshoglycerylation, which might be related to signaling or energy metabolism. Among the 3 missing thiols, mercaptolactate and mercaptopyruvate were detectable in MS1 scans but yield no usable MS/MS spectra because of limited intensity; the rest one, polysulfide, exhibited variable molecular compositions all with low endogenous concentrations. Taken together, thiol-chromene click chemistry enabled live-cell labeling to substantially expand thiol coverage, paving way for pathway analysis in thiol metabolism.

Key figures of merit for thiol quantification were evaluated to validate the analytical performance of this method. Absolute quantification of 12 thiols was accomplished by performing UPLC-MS with

https://doi.org/10.1038/s41467-026-70336-z

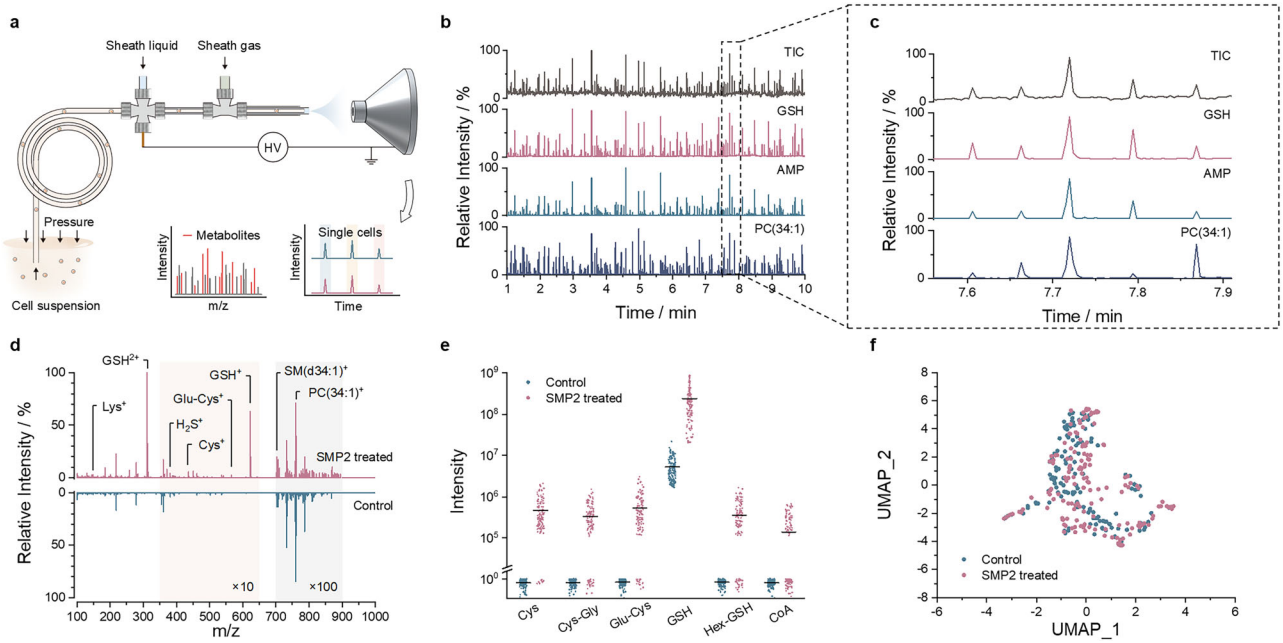

Fig. 3 | Integration of organic mass cytometry and live-cell labeling. **a** Construction and workflow of organic mass cytometry. **b**, **c** Time-resolved single-cell events which present as pulsed peaks in TIC and EICs and their zoom-in. **d** Mass spectra of **SMP2**-treated and -untreated (control) single HeLa cells in positive mode. **e** Comparison of MS responses of thiols from single HeLa cells treated with **SMP2** ($n = 121$ cells) and without **SMP2** ($n = 147$ cells). Hex-GSH: hexosyl-glutathione. The horizontal line represents the mean. **f** UMAP of single-cell metabolomic data in positive mode from **SMP2**-treated group ($n = 160$ cells) and control group ($n = 147$ cells). Source data are provided as a Source Data file.

SMP2-labeled NACA as IS. To cover a broad concentration range, segmented calibration curves were constructed across 100 pM–100 nM and 100 nM–20 μM with good linearity (Supplementary Fig. 5 and Supplementary Table 1). The estimated limit of detection (LOD) varied from 1.60 pM to 27.9 pM, and recovery ranged from 92.7 to 116.7%, depending on thiol species (Supplementary Table 2). We then evaluated repeatability of the method through precision measurements, which yielded intraday and interday relative standard deviations (RSDs) <8.1% and <8.9%, respectively (Supplementary Table 2). The intracellular concentrations of 12 thiols were simultaneously determined based on chromatographic peak area ratio (labeled thiols/IS) in conjunction with the calibration curves (Supplementary Table 3). Specially, GSH reached a high concentration of 4.64 mM, which was consistent with the requirement to maintain the reductive cellular environment and agreed with previously reported levels (0.5–10 mM)[31]. Collectively, this chemical labeling strategy provided a reliable approach for quantification of multiple thiols with excellent accuracy and precision.

The labeling effectiveness were then evaluated by contrasting different strategies. We first compared the MS response of thiols with and without labeling. Living cells were treated with either **SMP2** or DMSO, and thiols (labeled or not) were subsequently quantified using UPCL-MS with SMP2-labeled NACA as IS. As expected, MS signals of labeled thiols increased by orders of magnitude relative to unlabeled thiols (Fig. 2e). We further compared the labeling efficiency under various labeling conditions: in living cells, in lysates and in lysates with TCEP (Fig. 2f). In general, live-cell labeling demonstrated superior performance compared to the others. When labeling in cell lysates, the universal decrease in thiol signals was observed and could be ascribed to inevitable oxidation accompanying lysis. With the addition of TCEP, no substantial improvement was realized, but endogenous disulfides like oxidized glutathione (GSSG) were misidentified as free thiols, which was responsible for the unexpected increase of GSH in the TCEP-treated group. These results demonstrated that live-cell labeling could fundamentally prevent thiols from oxidation and underlined its remarkable superiority over other strategies.

Single-cell analysis based on organic mass cytometry

For the ultimate goal to profile thiol at single-cell level, we constructed and optimized organic mass cytometry platform[22,27] which was composed of four parts: cell sampling system, ESI interface (Supplementary Fig. 6), high resolution mass spectrometer (HRMS) and data processor (Fig. 3a). In detail, pressure injection system pumped cells which was suspended in MS-compatible buffer solution into the sampling capillary. Cells was mono-dispersed via Dean flow[33] and passed orderly into the ESI interface. They stayed alive[34] until metabolites were extracted by organic sheath liquid, followed by ionization with the assistance of sheath gas. Critical parameters of the interface were optimized for the best MS response of thiols (Supplementary Fig. 7). It took less than 1 s from metabolite extraction to MS detection, guaranteeing that acquired data reflected real-time status of cells. Subsequently, the data was analyzed by algorithm-based data processor which authenticated single-cell events from the temporal raw data and annotated each cell with corresponding metabolites. The untargeted single-cell metabolome library was established based on first UPLC-MS/MS identification at the population level and then algorithmic recognition at the single-cell level. In bulk HeLa cells, we totally detected 67407 molecular features and extracted 38822 MS/MS spectra from which 1176 metabolites were identified. Two metabolites of high intracellular levels, phosphatidylcholine PC(34:1) and phosphoryldimethylethanolamine, were selected as the indicators for single-cell events in positive and negative mode, respectively. From single-cell data, all the 1176 metabolites were screened, and the ones which met the threshold of precision and recall were admitted into single-cell metabolome library. Altogether, 224 and 131 metabolites (Supplementary Data 2 and 3) were identified from single HeLa cells in positive and negative mode, respectively.

We next evaluated the performance of the proposed method in efficiency, coverage, sensitivity, and compatibility. Extracted ion

https://doi.org/10.1038/s41467-026-70336-z

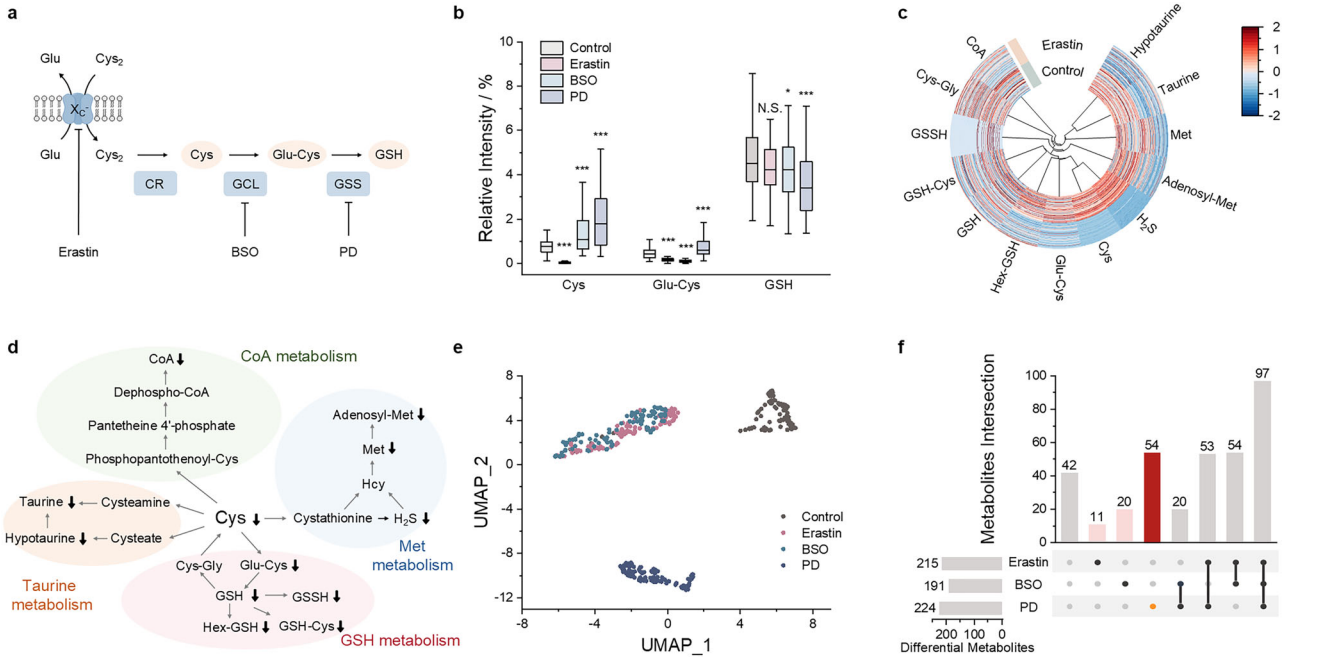

Fig. 4 | Metabolome profiling upon inhibition of GSH synthesis. a Biosynthesis pathway of GSH and three inhibitors of the engaged enzymes. **b** Thiol levels of single cells upon the treatment of DMSO, Erastin (Cys, $p = 1.14E\text{-}56$; Glu-Cys, $p = 4.97E\text{-}20$; GSH, $p = 5.09E\text{-}2$), BSO (Cys, $p = 9.99E\text{-}1$; Glu-Cys, $p = 1.65E\text{-}36$; GSH, $p = 2.01E\text{-}2$) and PD (Cys, $p = 1.00$; Glu-Cys, $p = 1.00$; GSH, $p = 2.47E\text{-}7$). Unpaired one-tailed Mann-Whitney rank sum tests are performed between inhibitors-treated cells and control cells. *: $p < 0.05$; **: $p < 0.01$; ***: $p < 0.001$. The box plot displays the median, upper and lower quartiles, and whiskers extending to 1.5 times the interquartile range. **c** Heatmap detailing z-scored normalized level of 13 thiols in Erastin-treated single cells and control. GSSH sulfanylglutathione. **d** Sulfur metabolic network constituted mainly of metabolism of CoA, taurine, GSH and Met, and intersecting at Cys. **e** UMAP depicting that three inhibitor-treated cells clusters into two group. **f** Comparison of differential metabolites of three inhibitors *vs.* control. In **b**, **c**, **d**, **f**, Control group, $n = 97$ cells; Erastin group, $n = 93$ cells; BSO group, $n = 103$ cells; PD group, $n = 105$ cells. Source data are provided as a Source data file.

chromatograms (EICs) of labeled GSH, adenosine monophosphate (AMP) and PC(34:1) (Fig. 3b) illustrated the excellent cell throughput which profited from continuous cell injection with the maximum rate of 50 cells min^{-1}. As depicted in the enlarged EICs, single-cell events that presented as pulsed peaks were almost uniformly distributed along the time axis and different metabolites inside the same cell kept accordant with each other (Fig. 3c). Mass spectra of single HeLa cells (Fig. 3d and Supplementary Fig. 8) displayed the diversity of identified metabolites, including amino acids, nucleotides, monosaccharides and lipids. Before labeling, only GSH among all the endogenous thiols was directly detected, whereas the number of thiols ascended to 27 after **SMP2** treatment (Fig. 3e and Supplementary Table 1). Meanwhile, labeled GSH at *m/z* 311.6308 emerged astonishingly as the most intense peak across the entire mass spectrum (Fig. 3d). It is also worth noting that hydrogen sulfide was detected in the form of **SMP2-SO_3H** of which only one site was captured by SMP2 due to steric hindrance and the other was oxidated in ESI. Sulfite is the other source of **SMP2-SO_3H** as confirmed by standards analysis (Supplementary Fig. 9), which was also consistent with the reported reactivity of chromene[35]. This phenomenon was consistent with the UPLC-MS/MS results obtained from bulk cell analysis (Supplementary Fig. 10) and again emphasized the necessity of live-cell labeling. Additionally, applying this method to Jurkat cells demonstrated its utility in suspension cell lines (Supplementary Fig. 11). To investigate whether **SMP2** significantly interfere with the global metabolism, data dimensionality reduction employing uniform manifold approximation and projection (UMAP) of single-cell metabolomic data was performed (Fig. 3f and Supplementary Fig. 12). The clusters of SMP2-treated cells and -untreated cells overlapped with each other, indicating that no significant metabolomic difference was discriminated between two groups. These findings showed that the integration of live-cell labeling and organic mass cytometry provided a powerful tool for simultaneous profiling of thiols and other metabolites at the single-cell level.

Metabolic fluctuation upon inhibition of GSH synthesis

To evaluate practicability and accuracy of this integrated methodology, perturb and observe (P&O) tests were introduced to monitoring fluctuation of thiols and other metabolites. GSH synthesis has been well-characterized: cystine (Cys_2) was imported into cells via cystine/glutamate antiporter system (X_c^-) and converted into Cys by cystine reductase (CR); glutamate (Glu), Cys and glycine (Gly) are ligated sequentially by glutamate cysteine ligase (GCL) and glutathione synthetase (GSS) (Fig. 4a). Three small-molecule compounds were selected to inhibit key enzymes in GSH synthesis and changes of three involved thiols (Fig. 4b) were measured by organic mass cytometry. The treatment duration of 2 h[4] was chosen to avoid that prolonged accumulation of reactive oxygen species (ROS) led to metabolic dysfunction which might interfere with thiol metabolism in turn. Erastin was reported to induce ferroptosis through inhibition of Cys_2 uptake, thereby depleting GSH[4]. Treating HeLa cells with Erastin led to uniform decrease of Cys and downstream Glu-Cys but did not yet significantly affect GSH due to limited treatment duration, consistent with its biochemical features. Besides, Cys accumulation and Glu-Cys depletion were observed simultaneously when replacing Erastin with buthionine sulfoximine (BSO), another ferroptosis inducer which blocks the ligation between Glu and Cys[36]. Polydatin (PD), a bioactive constituent separated from *Reynoutria japonica Houtt.* with antitumor activity[37], has recently been proved to inhibit GSS in vitro and in living cells[38]. After the treatment of PD, GSH diminished significantly while Cys and Glu-Cys accumulated. The obtained results revealed that even subtle and local changes in thiol metabolism could be readily uncovered with this integrated method.

We further extended our interests in all sulfur-containing metabolites. Given that Cys serves as the vehicle for sulfur conversion, Cys starvation could result in domino-like depression throughout entire sulfur metabolic network. As expected, 9 labeled thiols and 4 other sulfur-containing metabolites decreased significantly upon blocking Cys_2 uptake by Erastin (Fig. 4c). The two most responsive sulfur-containing species, Cys and hydrogen sulfide/sulfite, decreased synchronously by more than thirtyfold, evidencing their rapid interconversion. The only different case that Gly-Cys level maintained constant was ascribed to the joint effect of upregulated Cys replenishment from the GSH pool and decreasing GSH level. In fact, there was no exception for the end products of CoA, taurine, methionine (Met), and GSH pathways (Fig. 4d), which demonstrated the widespread sulfur starvation. Therefore, the detailed sulfur metabolic network was successfully mapped, profiting from unbiased detection of thiols and associated metabolites by organic mass cytometry.

As taking all intracellular species into account, we realized metabolome-wide comparison of changes stimulated by different inhibitors (Fig. 4e) using UMAP. Notably, treated cells fell into two distinct clusters that one involved Erastin and BSO and the other was assigned to PD. We identified totally 309 differential metabolites between the control group and inhibitor-treated groups based on the criteria of $|\log_2(\text{fold change})\ (\log_2(FC))| > 0.58$ and $p < 0.01$ (Supplementary Figs. 13–15). Again, PD-treated cells featured with more specific differential metabolites than the other groups though three groups shared 97 metabolites together (Fig. 4f). Among the PD-specific differential metabolites, the decreased AMP and guanosine monophosphate (GMP) (Supplementary Fig. 16) agreed with its inhibition of glucose-6-phosphate dehydrogenase (G6PD)[39], the limiting enzyme of pentose phosphate pathway. We attributed the commonality of three inhibitors to their similar function in GSH metabolism and correlated specific behaviors of PD with its multiple effects on G6PD, catalase (CAT)[40], interleukin-6 (IL-6)[41], etc. Comprehensive depiction of bioprocesses was achieved with the assistance of adequate molecular information provided by organic mass cytometry. Taken together, the employment of this method in P&O tests demonstrated its capability and extensibility in pathway activity monitoring, metabolic network mapping and untargeted metabolome profiling.

Metabolic heterogeneity of GSH pathway in RSL3-triggered ferroptosis

As the focus was transferred from GSH synthesis to its consumption, two anomalies aroused our interests. GSH serves as the cofactor of glutathione peroxidase 4 (GPX4) for the detoxification of hydroperoxides to corresponding alcohols and meanwhile itself is transformed into GSSG. RSL3, a canonical ferroptosis inducer, was confirmed to inactivate GPX4 and thereby elevate lethal lipid peroxidation[42]. However, GSH dramatically declined with the increasing treating time of RSL3 (Fig. 5a), which disobeyed the rule that metabolites accumulate (or keep constant due to negative regulation) while their consumption is blocked. Furthermore, projection of metabolomic data from control and treated cell pools by UMAP (Fig. 5b) showed that RSL3-treated cells clustered into two subtypes that one overlapped with control (subtype 1) and the other underwent apparent metabolic changes (subtype 2).

To figure out which pathways exerted predominant effect on the metabolic heterogeneity, we performed pathway enrichment analysis (Fig. 5c) of 182 differential metabolites between two subtypes (Supplementary Fig. 17). GSH metabolism, ether lipid metabolism and glycerophospholipid metabolism emerged as the top three pathways differing between these subtypes. Especially, we observed the bimodal distribution of GSH levels in RSL3-treated cells (Fig. 5d) where subtype 1 was nearly equivalent to control whereas subtype 2 declined significantly, responsible for the time-dependent reduction of GSH described above. Detailed comparison of labeled thiols suggested that subtype 2 exhibited downregulation across the entire GSH synthesis pathway (Fig. 5e), disagreeing with the known effect of RSL3 on GSH metabolism. To monitor de novo GSH synthesis, deuterated cystine (Cys_2-*d*4) was chosen to label the involved thiols as Cys-*d*2, Glu-Cys-*d*2 and GSH-*d*2 (Supplementary Fig. 18a). RSL3-pretreated cells were pulse labeled with Cys_2-*d*4 and **SMP2** simultaneously and then analyzed by the established method[27]. Results showed that subtype 1 presented higher labeling extent of GSH than subtype 2, revealing that subtype 2 underwent low activity of de novo GSH synthesis (Supplementary Fig. 18b). As to lipid metabolism, the levels of phospholipids, particularly those composed of polyunsaturated fatty acid (PUFA), decreased significantly in subtype 2 as compared with those in subtype 1 (Fig. 5f). Coincidentally, GSH depletion and lipid dysmetabolism were respectively the inducement and the hallmark of ferroptosis. These observations supported the preliminary conclusion that HeLa cells were comprised of two subpopulations, RSL3-resistant (subtype 1) and RSL3-sensitive (subtype 2), and in RSL3-sensitive cells, ferroptosis was triggered through downregulation of GSH synthesis.

However, how did RSL3 inhibit GSH synthesis and what determined metabolic heterogeneity in RSL3-triggered ferroptosis remained unclear. NRF2, a transcription factors which regulates multiple pathways to counteract detriment from ROS and electrophiles, promotes GSH synthesis and regeneration through upregulating X_c^-, GCL and glutathione reductase (GSR)[43], namely NRF2-GSH axis. Inhibition of NRF2 was reported to facilitate ferroptosis in macrophage and cancer cells[44,45], especially the ones resistant to RSL3[46]. Moreover, similar bimodal distribution of GSH was recently reported to be driven by differential expression of NRF2 in two subpopulations of aging stem cells[47]. Inspired by this, we put forward the hypothesis (Fig. 5g): (i) RSL3 downregulated GSH synthesis by inhibiting NRF2, directly or not; (ii) the NRF2 level differed in two subtypes, which resulted in metabolic heterogeneity.

Cross-validation was performed for the proposed hypothesis. As an alternative method, we utilized ThiolTracker, a live-cell fluorescent probe for GSH, to depict GSH distribution with fluorescence-based flow cytometry and yielded consistent results (Fig. 5h) with organic mass cytometry. Two subtypes were separately collected using fluorescence activated cell sorting (FACS), and key proteins involved in GSH metabolism were subsequently quantified by western blot (Fig. 5i). As we expected, NRF2 and downstream X_c^-, GCLC (catalytic subunit of GCL), GSR differed between two subtypes. In detail, subtype 1 downregulated NRF2, X_c^-, and GCLC as compared with control, responsible for uniform decrease of Cys, Glu-Cys, and GSH. On the contrary, the level of NEF2 in subtype 2 was comparable to that in control, resulting in similarly unaltered levels of downstream proteins and GSH. These evidences supported our hypothesis that the differential expression of NRF2 resulted in metabolic heterogeneity of GSH when NRF2 was downregulated by RSL3.

Discussion

We described thiol-chromene click chemistry for the exploitation of mass SMPs which covalently bonded to intracellular thiols with high specificity and biocompatibility. Caging sulfhydryl groups inside living cells guaranteed accurate mapping of the measured thiol levels to their native concentrations, while the introduction of charged labels significantly enhanced the detection sensitivity, thereby expanding thiol coverage. By comparing labeling results, we emphasized the importance of live-cell labeling rather than labeling after lysis during which process thiols suffered multi-sourced oxidation. The employment of reductants could not regenerate thiols from sulfonate but cause ambiguity between thiols and endogenous disulfides. It was also demonstrated that impermanently charged ammoniums exhibited superior membrane permeability as compared with the permanently charged ones, as the latter experienced more repulsion from the hydrophobic lipid bilayer while the former

https://doi.org/10.1038/s41467-026-70336-z

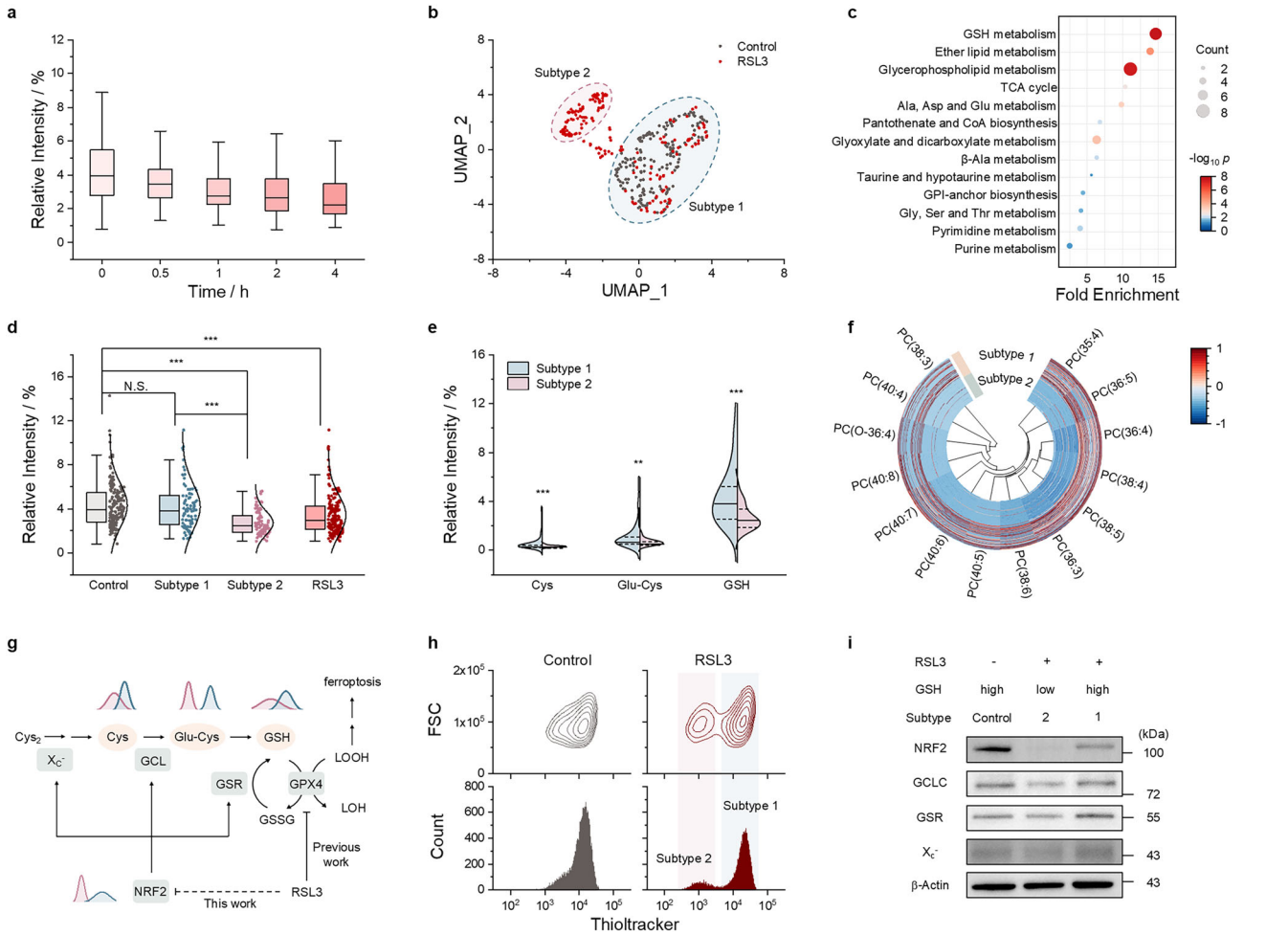

Fig. 5 | Investigation of RSL3 induced heterogenous GSH metabolism. a GSH level in single HeLa cells with increasing treating time of 2 μM RSL3 (0 h, $n = 182$ cells; 0.5 h, $n = 182$ cells; 1 h, $n = 189$ cells; 2 h, $n = 184$ cells; 4 h, $n = 207$ cells). The box plot displays the median, upper and lower quartiles, and whiskers extending to 1.5 times the interquartile range. **b** UMAP depicting the heterogeneity of RSL3-treated HeLa cells. **c** Pathway enrichment analysis of differential metabolites of subtype 1 *vs.* subtype 2. One-tailed hypergeometric tests are performed without adjustments, and only pathways with $p < 0.05$ are shown. **d** Distribution of GSH levels in control, RSL3 group and its subtypes. $p = 5.01E\text{-}7$ for RSL3 *vs.* Control, $p = 4.41E\text{-}1$ for Subtype 1 *vs.* Control, $p = 9.00E\text{-}14$ for Subtype 2 vs. Control, $p = 1.24E\text{-}7$ for Subtype 1 *vs.* Subtype 2. Unpaired two-tailed Mann-Whitney rank sum tests are performed. The box plot displays the median, upper and lower quartiles, and whiskers extending to 1.5 times the interquartile range. **e** Comparison of Cys ($p = 5.98E\text{-}4$), Glu-Cys ($p = 6.45E\text{-}3$), and GSH ($p = 6.24E\text{-}8$) levels between two subtypes ($n = 84$ cells for subtype 1 and $n = 87$ cells for subtype 2) with one-tailed Mann-Whitney rank sum tests. **f** Heatmap detailing z-scored normalized level of 14 lipids in two subtypes. **g** The hypothesized pathway in which RSL3 inhibits GSH synthesis and regeneration and triggers metabolic heterogeneity of GSH. **h** Flow cytometric contour plots (top) and histograms (bottom) of RSL3-treated cells and control which are incubated with 10 μM ThiolTracker for 30 min. FSC forward scatter. **i** Immunoblot analysis for expression of NRF2, GCLC, GSR, and X_C^- in two subtypes of RSL3-treated cells and control. Similar results were obtained in two independent biological replicates. In **b**–**f**, control, $n = 182$ cells; RSL3 group, $n = 171$ cells; subtype 1, $n = 84$ cells; subtype 2 $n = 87$ cells. In **d**, **e**, *: $p < 0.05$; **: $p < 0.01$; ***: $p < 0.001$. Source data are provided as a Source data file.

could deprotonate and diffuse across the membrane in a neutral form. Since ionization efficiency rises with the increasing substitution number of ammoniums, while reactivity declines along the same change, tertiary ammoniums achieved the maximum ionization efficiency and minimum reactivity, namely biochemical interference, among impermanently charged ammoniums, which makes them ideal charged labels for live-cell applications.

While both untargeted metabolome profiling and targeted metabolite analysis have been independently achieved at the single-cell resolution[48], their integration has not been previously realized. Unfortunately, due to manipulative difficulties and inevitable sample loss, it is impractical to segment individual mammalian somatic cells separately for untargeted profiling and targeted analysis, which bulk analysis always does[49]. This limitation hinders the comprehensive yet precise understanding of metabolic heterogeneity. This challenge could be circumvented by the employment of organic mass cytometry which enables unbiased detection of both predefined targets and other metabolites. Hence, as integrating thiol labeling with organic mass cytometry, we achieved comprehensive yet detailed depiction of bioprocesses at the single-cell level: thiol fluctuation upon inhibition of glutathione synthesis was successfully monitored; sulfur metabolic network mapping and metabolome-wide comparison of inhibitor-induced changes demonstrated capability and extensibility of the proposed method.

The single-cell thiol profiling revealed that RSL3 triggered unusual GSH decrease and heterogeneous GSH metabolism in HeLa cells. The mechanism behind this phenomenon was synergistically clarified by multimodal analysis based on both MS and fluorescent techniques. The results supported the hypothesis that RSL3 inhibited the entire GSH synthesis pathway through its downregulation to NRF2. Additionally, RSL3 induced differential expression of NRF2 between two subtypes, which was transmitted along the NRF2-GSH axis[43] and finally

resulted in bimodal distribution of GSH. These findings suggested a potential connection between RSL3 and NRF2 which has not been thoroughly explored. Ubiquitin-specific-processing protease 11 (USP11) was reported to bridge the gap between RSL3 and NRF2 in the manner that RSL3 directly inhibits USP11[50], and USP11 stabilizes NRF2 by deubiquitination[51]. This provides a possible mechanism elucidation for RSL3-triggered GSH depletion, though direct and detailed validation awaits further investigation. Besides, GSH response to RSL3 seems to be cell line-dependent: RSL3 downregulated GSH in U251 and U287 glioma cells[52], PC-3 and DU145 prostatic adenocarcinoma cells[53] and BEAS-2B bronchial epithelioid cells[54]; whereas the intracellular GSH level remained unchanged in MDA-MB-231 breast carcinoma cells[55], A549 lung adenocarcinoma cells[56] and BJeLR foreskin fibroblast cells[42] following RSL3 treatment. The underlying (epi)genetic differences and detailed molecular mechanisms remain to be further explored.

RSL3-induced heterogeneous GSH metabolism in HeLa cells is not an isolated case. During skeletal muscle stem cells aging, differential expression of NRF2 drove a bimodal distribution of GSH level[47], sharing a similar mechanism with metabolic heterogeneity in RSL3-triggerred ferroptosis. Besides, population-averaged measurements revealed that four heterologous subtypes of triple-negative breast cancer (TNBC) cells[57] exhibited ferroptosis heterogeneity featured with divergent GSH metabolism. Similar to subtype 2, the luminal androgen receptor (LAR) subtype was much more sensitive to RSL3 than other three subtypes, based on which an immunotherapy combination strategy was proposed and evidenced with high therapeutic efficacy for LAR tumors[58]. Given that heterogeneous GSH metabolism has been demonstrated in divergent bioprocesses and multiple cell lines, thiol profiling at the single-cell level shows great promise for the exploitation of novel therapies for related diseases, including cancer, neurodegeneration and atherogenesis.

In conclusion, we developed an integrated methodology for single-cell thiol profiling to investigate heterogeneous GSH metabolism triggered by RSL3. Live-cell labeling energized by chromene-thiol click chemistry guaranteed authenticity and sensitivity of thiol analysis, while organic mass cytometry provided an efficient and unbiased detection method for both thiols and metabolites within single cells. Their integration showed excellent practicability and capability in pathway activity monitoring, metabolic network mapping and untargeted metabolome profiling. Through thiols monitoring at the single-cell resolution, we uncovered metabolic heterogeneity of GSH in RSL3-triggered ferroptosis and proposed the underlying mechanism that RSL3 induced differential expression of NRF2 and resulted in heterogeneous downstream metabolism. To the best of our knowledge, this study represents the first attempt to simultaneously profile both targeted and untargeted single-cell metabolome. Further extensions employing diversified labeling strategies could advance the investigation of dynamic and labile metabolic processes across various species, pathways and even subcellular locale.

Methods

Cell lines and cell culture

HeLa (CCL-2), NE-4C (CRL-2925) and Jurkat (TIB-152) cell lines were originally obtained from the American Type Culture Collection (ATCC) and verified to be free of mycoplasma contamination. HeLa were grown at 37 °C with 5% CO_2 in Dulbecco's modified eagle medium (DMEM, Gibco) supplemented with 10% (*V/V*) fetal bovine serum (FBS, Viva Cell), 100 U mL^{-1} penicillin and 100 U mL^{-1} streptomycin (Macklin). NE-4C were grown at 37 °C with 5% CO_2 in minimum essential medium (MEM, Gibco) supplemented with 10% (*V/V*) FBS (Viva Cell), 1 mM sodium pyruvate (Gibco), 2 mM alanyl-glutamine (Gibco), 100 U mL^{-1} penicillin and 100 U mL^{-1} streptomycin (Macklin). The cells were seeded at 10^6 cells per 60 mm dish and subcultured every 1–2 days when they reached approximately 70% confluency.

Cell proliferation and cytotoxicity assay

Cells were seeded into a 96-well plate at the concentration of approximately 5×10^3 cells per well and incubated at 37 °C with 5% CO_2. Twelve hours after seeding, cells were gently washed with DPBS (Gibco) three times and then incubated with varying concentrations of **SMP2** in FBS-free culture for 1 h. Each well was again washed with DPBS three times and then incubated with 4 mM MTS (Bestbio) for 1 h. Absorbance (490 nm) of each well was measured using the plate reader Synergy H1 (BioTek) for calculation of the cell viability.

Metabolites extraction from bulk cells

A 10 mm dish of cells were washed with DPBS three times when they reached approximately 70% confluency. After being quenched with 2 mL of prechilled 1:1 (*V/V*) methanol-water, cells were harvested and homogenized using sonic dismembrator JY92-II (Scientz) with ice-water bath. Lysates were then centrifuged at 10,000 × *g* for 10 min at 4 °C using the centrifuge MG1650 (Merrick). The supernatant was collected as aqueous extracts while the pellets were added with 2 mL of prechilled 3:1 (*V/V*) dichloromethane-methanol to extract nonpolar metabolites. The same homogenization and centrifugation were performed to obtain organic extracts. Both supernatants were dried under N_2 for 30 min and then evaporated at 45 °C for 4 h using a centrifugal evaporator SPD111V (Thermo). The dried aqueous and organic extracts were stored at −80 °C until UPLC-MS(/MS) analysis.

Thiol labeling with SMPs

For live-cell labeling, cells were incubated with 80 μM SMPs in FBS-free culture for 10 min and washed with DPBS three times both before and after SMP incubation.

In single-cell analysis, adherent and suspension cells were processed differently: adherent cells were trypsinized and resuspended in 140 mM ammonium formate buffer solution, while suspension cells were directly resuspended in the buffer solution after labeling and washing. For Cys_2-d_4 labeling, cells were incubated with 200 μM Cys_2-*d*4 and 80 μM SMP2 in FBS-free and unlabeled Cys_2-free culture for 10 min. Subsequent steps were performed as described for the non-isotopic experiments.

As to bulk analysis, aqueous extracts from lysates which was prepared as described above was sampled to UPLC-MS/MS. For labeling in lysates, 80 μM **SMP2** was added into lysates. In case of labeling under reducing circumstance, additional 20 μM TCEP was used. In quantitative analysis, 100 nM **SMP2**-labeled NACA, which was obtained by mixing NACA with 10 eq. **SMP2**, was added into cell lysates as the IS.

As to thiol standards labeling, 12 thiol standards (Methanethiol, Cysteamine, Mercaptoacetamide, Mercaptoacetic acid, Cys, Hcy, Acetyl-Cys, Cys-Gly, Glu-Cys, Pantetheine, GSH, Dephospho-CoA) were first combined to prepare a mix stock solution with each thiol at 10.0 mM. TCEP equivalent to total thiols was added to the solution to maintain the reduced state of thiols. The stock solution was then diluted to a concentration series (100 pM, 200 pM, 500 pM, 1 nM, 2 nM, 5 nM, 10 nM, 20 nM, 50 nM, 100 nM, 200 nM, 500 nM, 1 μM, 2 μM, 5 μM, 10 μM, 20 μM), followed by labeling with 80 μM **SMP2**. Finally, 100 nM IS was added to the concentration series.

Treatment of inhibitors

Cells were washed with DPBS three times when they reached approximately 70% confluency. To inhibit GSH synthesis at different node, cells were separately treated with DMSO, 20 μM Erastin, 200 μM BSO and 200 μM PD in culture medium for 2 h. In RSL3 treatment assay, cells were treated with 5 μM RSL3 in culture medium for 0–4 h. All the cells were washed with DPBS three times again before subsequent single-cell analysis.

FACS

HeLa cells were washed with DPBS three times before being treated with 10 μM ThiolTracker Violet (Thermo) in FBS-free culture for 30 min. The treated cells were washed with DPBS three times again, trypsinized and resuspended in DMEM solution with 3% (*V/V*) FBS. FACS was performed on an Aria III flow cytometer (BD Biosciences), and BV510 channel (450 nm/510 nm) was selected.

Western blot

Cells were lysed with RIPA buffer (Beyotime) for 10 min. Then the resulting mixture were centrifuged at 12,000 rpm for 10 min at 4 °C, and the supernatant was collected. Samples each containing 10 μg proteins were separated on 10% SDS-PAGE gels and transferred to PVDF membranes, which were subsequently blocked with 5% *w/V* BSA in TBST for 1 h. These membranes were incubated with primary antibodies overnight at 4 °C, followed by secondary antibodies for 1 h at room temperature. The X_c^- (12691S) primary antibody was purchased from Cell Signaling Technology, and NRF2 (ab62352), GCLC (ab190685), GSR (ab128933), β-Actin (ab8227) primary antibodies were purchased from Abcam.

UPLC-MS(/MS) analysis

UPLC-MS(/MS) was performed using ACQUITY UPLC I-Class (Waters) and Orbitrap Q Exactive Plus mass spectrometer (Thermo).

In untargeted metabolome profiling, two different columns, Amide and C8 (ACQUITY UPLC BEH, Waters, 2.1 × 100 mm^2, 1.7 μm), was applied respectively in the separation of aqueous extracts and organic extracts The column temperature of C8 was set at 50 °C and the other was set at 30 °C. The flow rate was 0.3 mL min^{-1}. Binary mobile phase (A, ACN; B, 95:5 (*V/V*) H_2O-ACN) was adopted with 1‰ (*V/V*) formic acid in positive-mode ESI or 1‰ (*V/V*) ammonium hydroxide in negative-mode ESI. In HILIC chromatography, the linear gradient was as follows: 0 min, 3% B; 1 min, 3% B; 6 min, 10% B; 20 min, 50% B; 25 min, 50% B. In reversed-phase chromatography, the linear gradient was as follows: 0 min, 0% A; 1 min, 0% A; 4 min, 40% A; 14 min, 80% A; 20 min, 99% A; 25 min, 99% A. All samples were resuspended in the initial mobile phase before submitting to the UPLC-MS detection. The UPLC separation was coupled to MS/MS system via electrospray ion source HESI-II (Thermo). The spray voltage of 3.5 kV and 4.0 kV was applied respectively in positive mode and negative mode. Other parameters in ESI were as follows: sheath gas flow rate, 35; aux gas flow rate, 10; sweep gas flow rate, 5; capillary temperature, 350 °C; S-lens RF level, 60. Full MS/dd MS2 (TOP5) mode was selected for MS/MS detection and detailed parameters were as follows: *m/z* range, 80–1200; resolution, 70000 for MS, 35000 for MS/MS; AGC target, 1×10^6 for MS, 1×10^5 for MS/MS; maximum injection time, 200 ms; isolation window, 0.4; dynamic exclusion, 30 s; fragmentation, NCE 10, 20, 30.

In thiol profiling, most parameters were the same as those in untargeted metabolome profiling except these mentioned below. T3 column (ACQUITY UPLC HSS, Waters, 2.1 × 100 mm^2, 1.7 μm) was applied in separation of labeled thiols and the column temperature was set at 30 °C. The linear gradient was as follows: 0 min, 0% A; 1 min, 0% A; 15 min, 15% A; 20 min, 15% A. The column temperature was set at 30 °C. Full MS/dd MS^2 (TOP5) mode was selected for qualitative analysis and Full MS mode was selected for quantitative analysis.

Fabrication of the organic mass cytometer

Cell sampling system, ESI interface, and HRMS constituted the organic mass cytometer.

Prior to sampling, cells were trypsinized and resuspended in 140 mM ammonium formate buffer solution (pH = 7.3–7.4), which kept cell alive and was MS-compatible. Cell suspension at the concentration of approximately 1×10^4 cells mL^{-1} was magnetically stirred to maintain a homogeneous state. The suspension was pumped by pressure injection cell PC77 MAG (Next Advance) into the sampling capillary (I.D., 50 μm; O.D., 150 μm) with N_2 at the pressure of 0.3 MPa. Via several loops with the diameter of 2 cm in the sampling capillary, cells were orderly arrayed and finally reached the ESI interface.

At the interface (Supplementary Fig. 6), two junctions assembled three coaxial capillaries which varied in diameters. Cell suspension flowed inside the inner capillary (sampling capillary), sheath fluid (methanol supplemented with 1‰ (*V/V*) formic acid in positive mode or 1‰ (*V/V*) ammonium hydroxide in negative mode) passed through the in-between capillary (I.D., 250 μm; O.D., 365 μm) with the flow rate of 15 μL min^{-1} and sheath gas was introduced inside the outer capillary (ID, 530 μm; OD, 680 μm) at the pressure of 0.7 MPa. The inner capillary was approximately 2 mm shorter than the in-between capillary for sufficient mixture between cell suspension and sheath liquid. The outer capillary was approximately 5 mm shorter than the in-between capillary to maintain a steady spray. The voltage of 4.5 kV was applied between sheath liquid and the inlet of mass spectrometer for both polarity modes. Other parameters in ESI (HESI-II) were as follows: aux gas flow rate, 0; sweep gas flow rate, 0; capillary temperature, 275 °C; S-lens RF level, 50.

The mass spectrometer Orbitrap Q Exactive Plus was employed in the data acquirement of single cell analysis. In MS scanning, full MS mode was selected and detailed parameters were as follows: *m/z* range, 80–1200; resolution, 70,000; AGC target, 1×10^6; maximum injection time, 50 ms.

Single cell data analysis

The single-cell metabolome information could be extracted by a four-step workflow based on algorithm: format transformation, EIC extraction, single-cell event authentication and normalization. Raw data was transformed into mzML format using ThermoRawFileParserGUI (Thermo) and imported into R with the package *RaMS*. EICs of given metabolites were then extracted from the compressed and complex three-dimension data. The ignored values were reassigned random numbers between 0 and 1, which did not disturb the following processing because intense peaks were larger than 10^5. PC(34:1) and phosphoryldimethylethanolamine were selected as the indicators for single-cell events in positive and negative mode, respectively. In detail, baseline and pulsed peaks in the EIC of indicators were distinguished by the package *baseline*. The peaks whose corrected intensity was three times higher than standard deviation of baseline were authenticated as single-cell events. Finally, MS intensity of each metabolite was normalized by dividing by the sum of MS intensity of all metabolites, including labeled thiols, inside the same cell. Of note, GSH could be directly detected without labeling, and consequently GSH existed in the labeled form in SMP2-treated cells and in the unlabeled form in control cells. These two forms showed markedly different MS sensitivity (Fig. 3e). Comparing the MS signals of two forms was biologically meaningless. Thus, GSH, labeled or not, was excluded from the normalization when comparing the metabolic difference between **SMP2**-treated cell and control (Fig. 3f and Supplementary Fig. 12.)

Statistics and reproducibility

Statistical analysis was conducted in R. Mann-Whitney rank sum tests were performed using function *wilcox.test*. Differential metabolites were identified based on two criteria: (1) $|\log_2(FC)| > 0.58$ and (2) $p < 0.01$. Pathway enrichment analysis was performed using the package *clusterProfiler*. The UMAP analysis was performed using the package *umap*. No statistical method was used to predetermine sample size. Cells whose indicator intensity was not three times higher than standard deviation of baseline were excluded. The experiments were not randomized. The investigators were not blinded to allocation during experiments and outcome assessment. Most experiments were

repeated independently three times with similar results. Western blots resulted from two independent experiments.

Metabolome library establishment

Both untargeted metabolome library and the thiol library were established first at the population level and then at the single-cell level.

In the establishment of untargeted metabolome library, UPLC-MS/MS data from bulk HeLa cells was processed by LipidSearch 5 (Thermo) and Compound Discoverer 3.3 (Thermo) for database searching and metabolite annotation. In total, 707 lipids and 469 other metabolites were identified with MS/MS confirmation. At the single-cell level, algorithm-based metabolites scanning was performed to confine the library. In detail, single-cell events were identified as described above and peaks in EICs of the 1176 metabolites were distinguished from the baseline in the same way. Metabolites would be admitted into the single-cell library once their peaks matched with single-cell events with precision >0.3 and recall >0.1. Metabolites with the same *m/z* yet different retention times were distinguishable in UPLC-MS analysis but not in organic mass cytometry. Thus, they were registered as single signals. The final library (Supplementary Data 2 and 3) was shown as the union of metabolites identified in different samples.

In the establishment of thiol library, UPLC-MS/MS data from bulk HeLa cells and NE-4C cells were analyzed manually. The MS/MS spectra with **SMP2**-characteristic ions at *m/z* 315.1705 and 270.1127 were extracted from raw data. The rest fragment ions in extracted spectra were first matched with the residues of endogenous compounds, usually amino acids, and then utilized to reconstitute entire structures of thiols. At the single-cell level, only thiols in HeLa were scanned and admitted into the single-cell library in the same way as the untargeted metabolome library did.

Reporting summary

Further information on research design is available in the Nature Portfolio Reporting Summary linked to this article.

Data availability

The metabolomic MS raw data have been deposited to MetaboLights with the dataset identifier MTBLS13900. The data that support the findings of this study are available in the supplementary material of this article. Source data are provided with this paper.

Code availability

The code developed in this manuscript has been submitted to Code Ocean[59].

References

1. Ryan, S. K. et al. Microglia ferroptosis is regulated by SEC24B and contributes to neurodegeneration. *Nat. Neurosci.* **26**, 12–26 (2023).
2. Niemann, B. et al. Oxidative stress and cardiovascular risk: obesity, diabetes, smoking, and pollution: part 3 of a 3-part series. *J. Am. Coll. Cardiol.* **70**, 230–251 (2017).
3. Hayes, J. D., Dinkova-Kostova, A. T. & Tew, K. D. Oxidative stress in cancer. *Cancer Cell* **38**, 167–197 (2020).
4. Dixon, S. J. et al. Ferroptosis: an iron-dependent form of non-apoptotic cell death. *Cell* **149**, 1060–1072 (2012).
5. Kang, N. et al. Stimuli-responsive ferroptosis for cancer therapy. *Chem. Soc. Rev.* **52**, 3955–3972 (2023).
6. Proneth, B. & Conrad, M. Ferroptosis and necroinflammation, a yet poorly explored link. *Cell Death Differ.* **26**, 14–24 (2019).
7. Fülöp, A. et al. New derivatization reagent for detection of free thiol-groups in metabolites and proteins in matrix-assisted laser desorption/ionization mass spectrometry Imaging. *Anal. Chem.* **92**, 6224–6228 (2020).
8. Rossi, R. et al. Blood glutathione disulfide: in vivo factor or in vitro artifact? *Clin. Chem.* **45**, 742–753 (2002).
9. Levison, M. E., Josephson, A. S. & Kirschenbaum, D. M. Reduction of biological substances by water-soluble phosphines: γ-globulin (IgG). *Experientia* **25**, 126–127 (1969).
10. Winterbourn, C. C. & Hampton, M. B. Thiol chemistry and specificity in redox signaling. *Free Radic. Bio. Med.* **45**, 549–561 (2008).
11. Yue, Y. K., Huo, F. J. & Yin, C. X. The chronological evolution of small organic molecular fluorescent probes for thiols. *Chem. Sci.* **12**, 1220–1226 (2021).
12. Huang, T. J., Armbruster, M. R., Coulton, J. B. & Edwards, J. L. Chemical tagging in mass spectrometry for systems biology. *Anal. Chem.* **91**, 109–125 (2019).
13. Lotto, J. et al. Single-cell transcriptomics reveals early emergence of liver parenchymal and non-parenchymal cell lineages. *Cell* **183**, 702–716 (2020).
14. Altschuler, S. J. & Wu, L. F. Cellular heterogeneity: do differences make a difference? *Cell* **141**, 559–563 (2010).
15. Li, Z. et al. Single-cell lipidomics with high structural specificity by mass spectrometry. *Nat. Commun.* **12**, 2869 (2021).
16. Zhu, H. Y. et al. Metabolomic profiling of single enlarged lysosomes. *Nat. Methods* **18**, 788–798 (2021).
17. Lombard-Banek, C. et al. In vivo subcellular mass spectrometry enables proteo-metabolomic single-cell systems biology in a chordate embryo developing to a normally behaving tadpole (X. laevis). *Angew. Chem. Int. Ed.* **60**, 12852–12858 (2021).
18. Passarelli, M. K. et al. The 3D OrbiSIMS-label-free metabolic imaging with subcellular lateral resolution and high mass-resolving power. *Nat. Methods* **14**, 1175–1183 (2017).
19. Yin, R. C. et al. High spatial resolution imaging of mouse pancreatic islets using nanospray desorption electrospray ionization mass spectrometry. *Anal. Chem.* **90**, 6548–6555 (2018).
20. Castro, D. C., Xie, Y. R., Rubakhin, S. S., Romanova, E. V. & Sweedler, J. V. Image-guided MALDI mass spectrometry for high-throughput single-organelle characterization. *Nat. Methods* **18**, 1233–1238 (2021).
21. Liu, Q. L. et al. High-throughput single-cell mass spectrometry reveals abnormal lipid metabolism in pancreatic ductal adenocarcinoma. *Angew. Chem. Int. Ed.* **60**, 24534–24542 (2021).
22. Shen, Z. et al. Dynamic metabolic change of cancer cells induced by natural killer cells at the single-cell level studied by label-free mass cytometry. *Chem. Sci.* **13**, 1641–1647 (2022).
23. Spitzer, M. H. & Nolan, G. P. Mass cytometry: single cells, many features. *Cell* **165**, 780–791 (2016).
24. Yao, H. et al. Label-free mass cytometry for unveiling cellular metabolic heterogeneity. *Anal. Chem.* **91**, 9777–9783 (2019).
25. Xu, S. T., Liu, M. X., Bai, Y. & Liu, H. W. Multi-dimensional organic mass cytometry: simultaneous analysis of proteins and metabolites on single cells. *Angew. Chem. Int. Ed.* **60**, 1806–1812 (2021).
26. Qin, S. J. et al. In-depth organic mass cytometry reveals differential contents of 3-hydroxybutanoic acid at the single-cell level. *Nat. Commun.* **15**, 4387 (2024).
27. Zhang, Y. et al. Dynamic single-cell metabolomics reveals cell-cell interaction between tumor cells and macrophages. *Nat. Commun.* **16**, 4582 (2025).
28. Huo, F. J. et al. Colorimetric detection of thiols using a chromene molecule. *Org. Lett.* **11**, 4918–4921 (2009).
29. Huo, F. J. et al. Chromene "lock", thiol "key", and mercury(ii) ion "hand": a single molecular machine recognition system. *Org. Lett.* **12**, 4756–4759 (2010).
30. Yang, Y. T. et al. Thiol-chromene "click" reaction triggered self-immolative for mr visualization of thiol flux in physiology and pathology of living cells and mice. *J. Am. Chem. Soc.* **142**, 1614–1620 (2020).

31. Meister, A. & Anderson, M. E. Glutathione. *Annu. Rev. Biochem.* **52**, 711–760 (1983).
32. Wang, L. F. et al. Fluorescent probes and mass spectrometry-based methods to quantify thiols in biological systems. *Antioxid. Redox Sign.* **36**, 354–365 (2022).
33. Kemna, E. W. M. et al. High-yield cell ordering and deterministic cell-in-droplet encapsulation using Dean flow in a curved microchannel. *Lab Chip* **12**, 2881–2887 (2012).
34. Shao, Y. L. et al. Intact living-cell electrolaunching ionization mass spectrometry for single-cell metabolomics. *Chem. Sci.* **13**, 8065–8073 (2022).
35. Zhong, K. L. et al. A colorimetric and NIR fluorescent probe for ultrafast detecting bisulfite and organic amines and its applications in food, imaging, and monitoring fish freshness. *Food Chem.* **438**, 137987 (2024).
36. Katoh, M., Hiratake, J., Kato, H. & Oda, J. Mechanism-based inactivation of E-coli gamma-glutamylcysteine synthetase by phosphinic acid- and sulfoximine-based transition-state analogues. *Bioorg. Med. Chem. Lett.* **6**, 1437–1442 (1996).
37. Söhretoglu, D., Baran, M. Y., Arroo, R. & Kuruüzüm-Uz, A. Recent advances in chemistry, therapeutic properties and sources of polydatin. *Phytochem. Rev.* **17**, 973–1005 (2018).
38. Chen, P. et al. High-throughput screening suggests glutathione synthetase as an anti-tumor target of polydatin using human proteome chip. *Int. J. Biol. Macromol.* **161**, 1230–1239 (2020).
39. Mele, L. et al. A new inhibitor of glucose-6-phosphate dehydrogenase blocks pentose phosphate pathway and suppresses malignant proliferation and metastasis in vivo. *Cell Death Dis.* **9**, 572 (2018).
40. Li, R. P. et al. Polydatin protects learning and memory impairments in a rat model of vascular dementia. *Phytomedicine* **19**, 677–681 (2012).
41. Ravagnan, G. et al. Polydatin, a natural precursor of resveratrol, Induces β-defensin oroduction and reduces inflammatory response. *Inflammation* **36**, 26–34 (2013).
42. Yang, W. S. et al. Regulation of ferroptotic cancer cell death by GPX4. *Cell* **156**, 317–331 (2014).
43. Tonelli, C., Chio, I. I. C. & Tuveson, D. A. Transcriptional regulation by Nrf2. *Antioxid. Redox Sign.* **29**, 1727–1745 (2018).
44. Namgaladze, D., Fuhrmann, D. C. & Brüne, B. Interplay of Nrf2 and BACH1 in inducing ferroportin expression and enhancing resistance of human macrophages towards ferroptosis. *Cell Death Discov.* **8**, 327 (2022).
45. Yang, J. W. et al. Cetuximab promotes RSL3-induced ferroptosis by suppressing the Nrf2/HO-1 signalling pathway in KRAS mutant colorectal cancer. *Cell Death Dis.* **12**, 1079 (2021).
46. Shin, D., Kim, E. H., Lee, J. & Roh, J. L. Nrf2 inhibition reverses resistance to GPX4 inhibitor-induced ferroptosis in head and neck cancer. *Free Radic. Biol. Med.* **129**, 454–462 (2018).
47. Benjamin, D. I. et al. Multiomics reveals glutathione metabolism as a driver of bimodality during stem cell aging. *Cell Metab.* **35**, 472–486 (2023).
48. Lu, H. Y., Zhang, H. & Li, L. J. Chemical tagging mass spectrometry: an approach for single-cell omics. *Anal. Bioanal. Chem.* **415**, 6901–6913 (2023).
49. Patti, G. J., Yanes, O. & Siuzdak, G. Metabolomics: the apogee of the omics trilogy. *Nat. Rev. Mol. Cell Biol.* **13**, 263–269 (2012).
50. Meng, C. J. et al. The deubiquitinase USP11 regulates cell proliferation and ferroptotic cell death via stabilization of NRF2 USP11 deubiquitinates and stabilizes NRF2. *Oncogene* **40**, 1706–1720 (2021).
51. Zhang, W. L. et al. The RSL3 induction of lung adenocarcinoma cell ferroptosis by inhibition of USP11 activity and the NRF2-GSH axis. *Cancers* **14**, 5233 (2022).
52. Chen, X. et al. SIRT1 activated by AROS sensitizes glioma cells to ferroptosis via induction of NAD plus depletion-dependent activation of ATF3. *Redox Biol.* **69**, 103030 (2024).
53. Fu, X., Wu, H. S., Li, C. J., Deng, G. & Chen, C. YAP1 inhibits RSL3-induced castration-resistant prostate cancer cell ferroptosis by driving glutamine uptake and metabolism to GSH. *Mol. Cell. Biochem.* **479**, 2415–2427 (2024).
54. Wang, L. L., Mai, Y. Z., Zheng, M. H., Yan, G. H. & Jin, J. Y. A single fluorescent probe to examine the dynamics of mitochondria-lysosome interplay and extracellular vesicle role in ferroptosis. *Dev. Cell* **59**, 517–528 (2024).
55. Li, P. Y. et al. Inhibition of cannabinoid receptor type 1 sensitizes triple-negative breast cancer cells to ferroptosis via regulating fatty acid metabolism. *Cell Death Dis.* **13**, 808 (2022).
56. Shui, S. F., Zhao, Z. L., Wang, H., Conrad, M. & Liu, G. Q. Non-enzymatic lipid peroxidation initiated by photodynamic therapy drives a distinct ferroptosis-like cell death pathway. *Redox Biol.* **45**, 102056 (2021).
57. Jiang, Y. Z. et al. Genomic and transcriptomic landscape of triple-negative breast cancers: subtypes and treatment strategies. *Cancer Cell* **35**, 428–440 (2019).
58. Yang, F. et al. Ferroptosis heterogeneity in triple-negative breast cancer reveals an innovative immunotherapy combination strategy. *Cell Metab.* **35**, 84–100 (2022).
59. Miao, D. Y. & Bai, Y. Single-cell thiol profiling enabled by live-cell labeling reveals metabolic heterogeneity in ferroptosis. Code Ocean. https://doi.org/10.24433/CO.9501996.v9501991 (2026).

Acknowledgements

This work was financially supported by the Natural Science Foundation of China (No. 22125401 to Y.B.) and the National Key R&D Program of China (2022YFC3400700 and 2023YFF1205900 to Y.B.).

Author contributions

Y.B. proposed the study concept and strategy. D.M. designed and performed the experiments and data analysis. Q.L. assisted with the data analysis of untargeted metabolome library. Y.Z. involved in the construction of organic mass cytometry. Y.W. and X.L. helped with the western blot experiments. Y.Z. and S.Q. involved in the discussion. D.M., Q.L., Y.Z., S.Q. and Y.B. wrote the manuscript.

Competing interests

The authors declare no competing interests.

Additional information

Supplementary information The online version contains supplementary material available at https://doi.org/10.1038/s41467-026-70336-z.

Correspondence and requests for materials should be addressed to Yu Bai.

Peer review information *Nature Communications* thanks Rosario M. Sanchez-Martin, who co-reviewed with Victoria Cano-Cortés, Tong Zhang, and the other anonymous reviewer(s) for their contribution to the peer review of this work. A peer review file is available.